

Fractional Chern Insulators in Twisted Bilayer MoTe₂: A Composite Fermion Perspective

Tianhong Lu¹ and Luiz H. Santos¹

¹Department of Physics, Emory University, 400 Dowman Drive, Atlanta, GA 30322, USA

(Dated: June 7, 2024)

The discovery of Fractional Chern Insulators (FCIs) in twisted bilayer MoTe₂ has sparked significant interest in fractional topological matter without external magnetic fields. Unlike the flat dispersion of Landau levels, moiré electronic states are influenced by lattice effects within a nanometer-scale superlattice. This study examines the impact of these lattice effects on the topological phases in twisted bilayer MoTe₂, uncovering a family of FCIs with Abelian anyonic quasiparticles. Using a composite fermion approach, we identify a sequence of FCIs with fractional Hall conductivities $\sigma_{xy} = \frac{C}{2C+1} \frac{e^2}{h}$ linked to partial filling ν_h of holes of the topmost moiré valence band. These states emerge from incompressible composite fermion bands of Chern number C within a complex Hofstadter spectrum. This approach explains FCIs with Hall conductivities $\sigma_{xy} = (2/3)e^2/h$ and $\sigma_{xy} = (3/5)e^2/h$ at fractional fillings $\nu_h = 2/3$ and $\nu_h = 3/5$ observed in experiments, and uncovers other fractal FCI states. The Hofstadter spectrum reveals new phenomena, distinct from Landau levels, including a higher-order Van Hove singularity (HOVHS) at half-filling, leading to novel quantum phase transitions. This work offers a comprehensive framework for understanding FCIs in transition metal dichalcogenide moiré systems and highlights mechanisms for topological quantum criticality.

Introduction– The experimental discovery of Fractional Chern Insulators (FCIs) [1–5] in twisted bilayer MoTe₂ (tMoTe₂) [6–9] has sparked significant interest in fractional topological matter without external magnetic fields in moiré transition metal dichalcogenide (TMD) systems.[10–14] The interplay of spin-orbit interaction, moiré layer potential, and interlayer tunneling in tMoTe₂ produces moiré valence bands with spin/valley-Chern numbers [12–15], providing a platform for the realization of FCIs with Hall conductivities $\sigma_{xy} = \nu_h e^2/h$ at hole filling $\nu_h = 2/3$ and $\nu_h = 3/5$ [6–9] when spontaneously broken time-reversal symmetry gives rise to partially filled spin-polarized Chern bands.

Although FCIs exhibit the same quantized transport properties as fractional quantum Hall states created by external magnetic fields [16], the microscopic origins of moiré bands and Landau levels are profoundly different. Landau levels exhibit flat dispersion because the magnetic length is significantly larger (nanometer scale) compared to the atomic separation (Angstrom scale) in conventional two-dimensional lattices. In contrast, moiré electronic states arise from the restructuring of electronic states within a superlattice with nanometer-scale periodicity [17], causing these states to be heavily influenced by lattice effects. In the dawn of the exploration of FCIs in TMD moiré systems, a burning question is to characterize the influence of such lattice effects on topological phases supporting fractional quasiparticles.

In this study, we uncover a family of FCIs supporting Abelian anyons in partially filled valence bands of tMoTe₂ and demonstrate how quantum phase transitions induced by lattice effects can change topological order. Employing a composite fermion approach [18–24] characterized by binding of two flux quanta of the Chern-Simons gauge field to electrons residing on a honeycomb lattice [25] describing the spin/valley polarized

Chern bands close to charge neutrality[12–15], we delineate a series of incompressible topological states at fractional filling $0 < \nu_h < 1$ of holes on the topmost spin-polarized valence bands of tMoTe₂. The flux attachment performed on the effective Haldane-type lattice [15, 25] yields a rich spectrum of fractal Hofstadter states[26] describing composite fermions coupled to a large dynamical Chern-Simons flux within each unit cell. The emergent Hofstadter spectrum, which constitutes a core aspect of our analysis, enables us to pinpoint emergent incompressible states, predict their fractional conductivities, and, notably, uncover new quantum critical phenomena that underscore key differences between composite fermions in Chern bands and Landau levels.

The main results of this work are:

- (1) We chart the sequence of FCIs with fractional Hall conductivity $\sigma_{xy} = \frac{C}{2C+1} \frac{e^2}{h}$, which originate from gapped composite fermion bands with integer Chern number C . Analysis of the composite fermion spectra reveals that the most robust incompressible states are those *Jain-FCI* states with fractional hole filling $\nu_h = \frac{C}{2C+1}$, which fit the pattern of hierarchical Jain states [18, 19]. Among these Jain-FCIs, we identify states at $\nu_h = 2/3$ and $\nu_h = 3/5$ consistent with recent experimental observation [6–9]. While the $2/3$ and $3/5$ states in tMoTe₂ were studied using a continuum composite fermion approach[27], we identify other classes of FCIs that deviate from the usual hierarchy, such as those at filling $\nu_h = \frac{1}{5}, \frac{2}{7}, \frac{4}{5}, \frac{6}{7}$, which exhibit, respectively, quantized transport $\sigma_{xy}/(e^2/h) = \frac{3}{5}, \frac{3}{7}, \frac{3}{5}, \frac{4}{7}$. Breaking away from the Landau-level paradigm, these *fractal-FCI* states arise from the development of small gaps in the fractal spectrum. The experimental observation of such fractal-FCIs would provide a signature of fractal composite fermions.
- (2) The principal Jain-FCI staircase converges to a compressible composite fermion state at half-filling ($\nu_h =$

1/2), which is characterized by a low-energy band with parabolic dispersion and an effective mass m^* . We analytically determine how m^* depends on the lattice parameters that define the effective Chern bands of tMoTe₂ and, unexpectedly, discover a higher-order Van Hove singularity (HOVHS) [28, 29] linked to the divergence of the effective mass. This phenomenon is distinct from the behaviors observed in half-filled Landau levels [30, 31] and other composite Fermi liquid approaches in tMoTe₂ [27, 32]. Remarkably, the proximity to this lattice-driven HOVHS of the half-filled compressible composite fermion band leads to the rapid collapse of the composite fermion gaps near half-filling, unveiling new mechanisms for quantum phase transitions between FCIs, which is one of the main results of this work. Leveraging this mechanism, we uncover several quantum phase transitions controlled by the hopping amplitudes. Thus, the composite fermion predictions offer a guiding principle for experimental and numerical exploration of novel FCIs and offer novel mechanisms for topological quantum criticality in transition metal dichalcogenide moiré systems.

Composite Fermions in tMoTe₂— For twist angle $\theta \lesssim 4^\circ$, the topmost valence bands of tMoTe₂ near each valley are topologically non-trivial bands with Chern numbers $C = \pm 1$ and spin-valley polarization $\sigma = \pm 1$. [12–15]. These isolated bands can be effectively described by a Haldane model [25] on a honeycomb moiré superlattice with sublattices A and B (denoted $\ell = \pm 1$), and (real) nearest and (complex) next-nearest neighbor hopping parameters [15],

$$H_\sigma = - \sum_{\ell=\pm 1} \sum_{\mathbf{r}, \mathbf{r}'} t_0 c_{\ell\sigma}^\dagger(\mathbf{r}) c_{-\ell\sigma}(\mathbf{r}') - \sum_{\ell=\pm 1} \sum_{\mathbf{r}} \sum_{\substack{\boldsymbol{\delta} \in \{\mathbf{a}_1, -\mathbf{a}_2, \\ \mathbf{a}_2 - \mathbf{a}_1\}}} t_1 e^{i\theta_\sigma^\ell} c_{\ell\sigma}^\dagger(\mathbf{r} + \boldsymbol{\delta}) c_{\ell\sigma}(\mathbf{r}) + \text{H.c.} \quad (1)$$

where $c_{\ell\sigma}^\dagger$ is the electron creation operator with spin σ , $\theta_\sigma^\ell = -2\pi\sigma/3$ is the Haldane phase, and $\mathbf{a}_1 = a(3/2, -\sqrt{3}/2)$, $\mathbf{a}_2 = a(3/2, \sqrt{3}/2)$ are the two primitive vectors (henceforth, we work in units of $a = 1$) connecting a site to its next-nearest neighbors as shown in Fig. 1. To capture the phenomenology of FCIs, we restrict our analysis to partially filled spin-valley polarized Chern bands resulting from the spontaneous breaking of time-reversal symmetry due to interactions [12–15] by focusing on electrons (holes) with fixed spin polarization $\sigma = -1$, with analogous results directly applying to the other spin-polarized state.

To establish convention similar to Refs. [6–9] reporting FCIs at hole filling ν_h of the highest valence band, we perform a particle-hole (PH) transformation $c_{\ell\sigma} \rightarrow c_{\ell\sigma}^\dagger$ that maps the parameters of the Hamiltonian (1) to

$$\{-t_0, -t_1, \theta_\sigma^\ell\} \xrightarrow{\text{PH}} \{t_0, t_1, -\theta_\sigma^\ell\}, \quad (2)$$

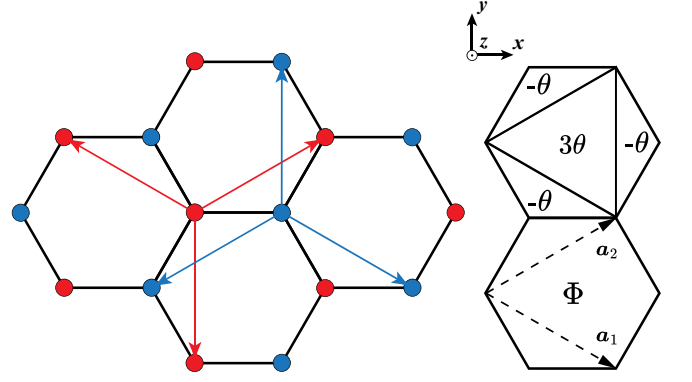


FIG. 1. Left: Honeycomb lattice with sublattices A ($\ell = 1$) in red and B ($\ell = -1$) in blue. The arrows denote the phase $e^{i\theta_\sigma^\ell}$ of the second-neighbor hopping term in the Hamiltonian (1). Time-reversal symmetry flips spin, changing the direction of the arrows. Right: The flux through the lattice along $+z$ direction, including the Haldane phase θ_σ^ℓ and the Chern-Simons flux $\Phi = \Phi_0 \cdot p/q$

which yields a tight-binding model for holes with hopping parameters t_0, t_1 and phase $\theta_\sigma^h = -\theta_\sigma^\ell = 2\pi\sigma/3$. In Fig. 2(a), we plot the valley-polarized bands for holes with Chern numbers $C = \pm 1$, for $t_0 = -1$ and $t_1 = -0.2$, consistent with Ref. [15] (see also [33]). The regime $0 < \nu_h < 1$ corresponding to partial filling of the lowest Chern band shown in Fig. 2(a) is the subject of this work.

We characterize the onset of incompressible states at partial band filling via a Chern-Simons flux attachment that maps a partially filled Chern band into a set of filled composite fermion bands [21–24]. Restricting our description to states with uniform particle density characterized by two flux quanta of the Chern-Simons gauge field attached to each electron, the uniform flux per unit cell Φ is proportional to the electron lattice filling $n \in [0, 1]$ (or the electron band filling $\nu_e = 2n \in [0, 2]$),

$$\Phi/\Phi_0 = 2 \cdot 2n = 2\nu_e = 2(2 - \nu_h), \quad (3)$$

where Φ_0 is the Chern-Simons flux quantum per unit cell (see Fig. 1), the coefficient of n in the first equality of Eq. (3) represents the product of 2 fluxes and 2 sublattices, and the last equality follows from charge conservation $\nu_e + \nu_h = 2$. We emphasize that, although we analyze the onset of incompressible composite fermion states by examining the Hofstadter spectrum of holes as a function of filling $0 < \nu_h < 1$, it is important to note that *Chern-Simons flux attachment is performed on electrons, not on holes*. This distinction is crucial because flux attachment to electrons accurately captures the FCI states observed in experiments, as we will discuss further. Additionally, we have verified that the Hofstadter spectrum of electrons exhibits the same Jain sequence at the corresponding electron filling $1 < \nu_e < 2$.

The Chern-Simons gauge field is incorporated into the

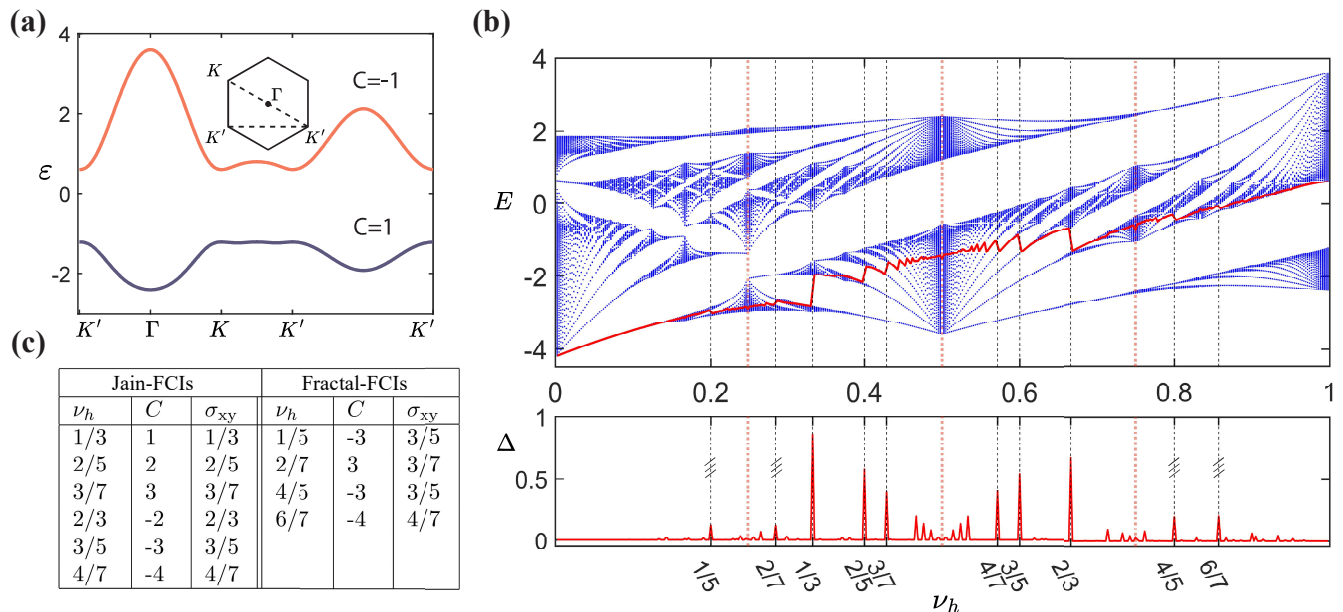


FIG. 2. $\theta_\sigma^h = -2\pi/3$, $t_0 = -1$, $t_1 = -0.2$. (a) Energy bands of Hamiltonian (1) after particle-hole transformation (2): Band gap $\Delta E = 1.8$; the lower (upper) band carries Chern number $C = 1$ (-1); (b) The Hofstadter spectrum: The energy spectrum E versus ν_h , and the red curve shows the Fermi surface (upper part). The composite fermion gap Δ (lower part). Red dashed lines show the $1/4, 1/2, 3/4$ hole fillings; (c) Fractional Hall conductance: table of Jain-FCI and fractal-FCI states at hole band filling ν_h .

effective model Eq.(1) using the Peierls substitution

$$t_{\mathbf{r},\mathbf{r}'} c_{\mathbf{r}}^\dagger c_{\mathbf{r}'} \rightarrow t_{\mathbf{r},\mathbf{r}'} e^{i(2\pi/\Phi_0) \int_{\mathbf{r}}^{\mathbf{r}'} d\mathbf{l} \cdot \mathbf{A}} c_{\mathbf{r}}^\dagger c_{\mathbf{r}'} \quad (4)$$

where \mathbf{A} is the Chern-Simons vector potential described by the gauge condition $\mathbf{A} = \frac{\Phi}{3\sqrt{3}/2}(x + \sqrt{3}y) \hat{e}_y$. More details are provided in the Supplemental Materials[34]. For rational values of the Chern-Simons flux $\Phi/\Phi_0 = p/q$ (with p and q coprime), the two Chern bands system splits into $2q$ composite fermion bands, resulting in the

The Chern number $C \in \mathbb{Z}$ [35] of the composite fermion insulator is related to the Hall conductance of the system as[21, 34]

$$\sigma_{xy} = \frac{C}{2C+1}. \quad (5)$$

Applying Eqs. (3) and (5) to composite fermion gaps shown in Fig.2(b), uncovers two classes of candidate FCIs in tMoTe₂. First, we identify FCI states where $\sigma_{xy} = \nu_h \frac{e^2}{h}$, dubbed Jain-FCI states for the analogy to hierarchical Jain states [18, 19] in Landau level systems. Alternatively, we also identify fractal-FCI states for which $\sigma_{xy} \neq \nu_h \frac{e^2}{h}$ that form due to the fractal bands distinct from Landau levels.

In Fig.2(b) and the left column of Fig.2(c), we depict a series of Jain-FCI states at hole filling $0 < \nu_h < 1$ for

Hofstadter spectrum of composite fermions shown in Fig.2(b). This spectrum has $\Phi \rightarrow \Phi + 6\Phi_0$ periodicity since the smallest triangle subunit pierced by flux shown in Fig.1 is $1/6$ of the unit cell area. We observe incompressible composite fermion states, indicated by vertical jumps in the composite fermion Fermi energies (red line in Fig.2(b)), occurring when integer bands are filled. This identifies composite fermion gaps Δ as a function of hole filling ν_h .

the hopping parameters $t_0 = -1, t_1 = -0.2$ based on Ref. [15]. Despite recent variations in the spectrum of Chern bands in tMoTe₂ observed in density functional methods [12–14], our results are robust for a range of hoppings. The most prominent gaps occur at $\nu_h = 1/3$ and $\nu_h = 2/3$, with particle-hole asymmetry observed between the two. Then, the composite fermion gap Δ decreases starting from the $2/5, 3/5$ hole filling towards $\nu_h = 1/2$. Notably, we identify Jain-FCIs at $\nu_h = 2/3, 3/5$, with the same topological properties as those recently observed [6–9]. Although a substantial $\nu_h = 1/3$ gap is indicated by the composite fermion approach, this FCI has so far not been seen in experiments, possibly due to other competing states. The Jain-FCI sequence extends and converges to half-filling, where the system becomes a composite Fermi liquid. Outside this region,

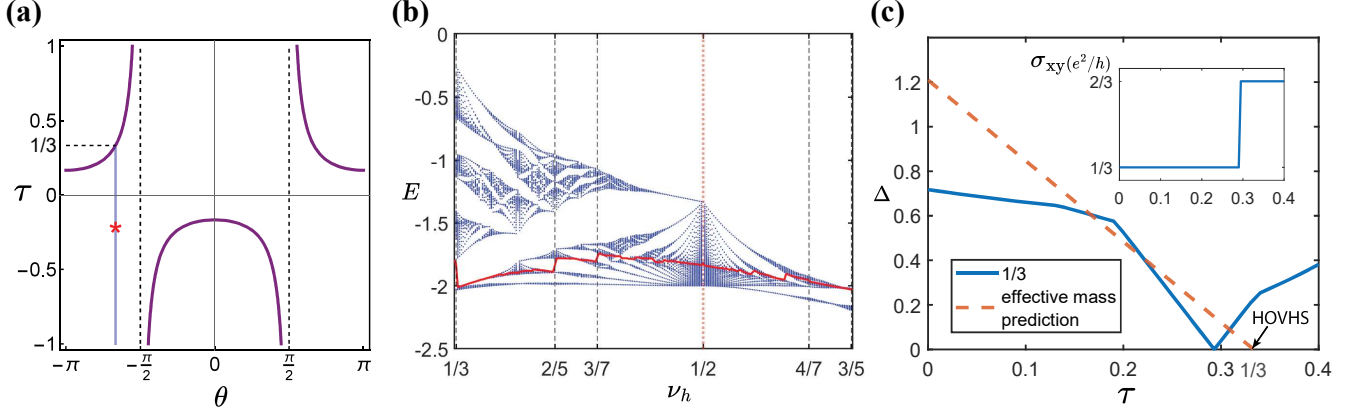


FIG. 3. Quantum phase transition correlated with the HOVHS at $\nu_h = 1/2$. (a) Curve shows the boundaries where the inverse of effective mass at $\nu_h = 1/2$ is 0, as a function of θ and $\tau = t_1/|t_0|$, the star symbol indicates the set of θ, τ used in Fig. 2(b); (b) The Hofstadter spectrum at $t_0 = -1, \tau = 1/3$ and $\theta = -2\pi/3$, zoomed in to show that the composite fermion gaps are nearly closed; (c) The composite fermion gap versus τ : the blue curve represents the gap at $\nu_h = 1/3$, while the orange dashed line represents the gap (8) predicted by the effective mass approach. This gap vanishes at $\tau = 1/3$ as the HOVHS emerges. The inset plots the transition of the Hall conductance σ_{xy} .

we identify fractal-FCI states shown on the right column of Fig. 2(c). These states originate from the fractal nature of the composite fermion spectrum and possess gaps significantly smaller than most of the Jain-FCI gaps such as the $\nu_h = 2/3$ and $\nu_h = 3/5$ FCI states. This indicates that observing fractal-FCIs may necessitate more stringent experimental conditions, such as lower temperatures or higher sample quality.

Quantum Phase Transition(QPT)– We now shift our attention to the states at half-filling ($\nu_h = 1/2$), to which the Jain sequence converges. The Chern-Simons flux per unit cell at $\nu_h = 1/2$ is $\Phi = 3\Phi_0$, and to gain

three Pauli matrices, and $\mathbf{k} = \frac{k_1}{2\pi}\mathbf{g}_1 + \frac{k_2}{2\pi}\mathbf{g}_2$ ($\mathbf{g}_1, \mathbf{g}_2$ are the reciprocal vectors). Direct analysis of the energy bands $\varepsilon_{\pm}(\mathbf{k}) = h_0(\mathbf{k}) \pm |\mathbf{h}(\mathbf{k})|$ shows that the lowest energy states near the band minimum have parabolic dispersion $\varepsilon_p \approx \varepsilon_0 + \mathbf{p}^2/(2m^*)$ with effective mass

$$m^* = \frac{m_0^*}{1 + 6\tau \cos \theta}, \quad (7)$$

where $m_0^* = 2\hbar^2/(3|t_0|)$ and $\tau = t_1/|t_0|$.

An intuitive account of the Jain-FCI states then follows. From Eq. (3), a small change in $\delta\nu_h = \nu_h - 1/2$ away from half-filling produces a perturbation in the Chern-Simons field δB according to $\delta\nu_h = \frac{1}{2}\delta\Phi/\Phi_0 = \frac{1}{2}\delta B \cdot \mathcal{A}_{u.c.}/\Phi_0$, where $\mathcal{A}_{u.c.} = \frac{3\sqrt{3}}{2}$ is the unit cell area. This extra field, in turn, gives rise to a Landau-fan with characteristic energy splitting

$$\Delta_{LL} = \hbar \frac{e\delta B}{m^*} = \frac{2\Phi_0}{\mathcal{A}_{u.c.}} \frac{\hbar e}{m^*} |\nu_h - 1/2|. \quad (8)$$

generality, we treat the Haldane phase as an independent variable θ . Then the compressible composite fermion states are described by the Hamiltonian $H_{\nu_h=1/2} = h_0(\mathbf{k})\sigma_0 + \sum_{i=1}^3 h_i(\mathbf{k})\sigma_i$ with [34]

$$\begin{aligned} h_0(\mathbf{k}) &= 2t_1 \cos \theta (\cos k_1 - \cos k_2 + \cos(k_1 - k_2)) \\ h_1(\mathbf{k}) &= t_0(1 - \cos k_1 + \cos k_2) \\ h_2(\mathbf{k}) &= t_0(-\sin k_1 + \sin k_2) \\ h_3(\mathbf{k}) &= 2t_1 \sin \theta (-\sin k_1 - \sin k_2 + \sin(k_1 - k_2)) \end{aligned} \quad (6)$$

where σ_{μ} ($\mu = 0, 1, 2, 3$) represents the 2×2 identity and

This Landau fan structure is clearly seen in Fig. 2(b), and Eq. (8) provides the correct energy scales as $\nu_h \rightarrow \frac{1}{2}$. [34] Furthermore, according to Eq. (8), $\Delta_{LL} \rightarrow 0$ as $m^* \rightarrow \infty$, when the band curvature vanishes near the minimum, signaling the onset of a higher order Van Hove singularity (HOVHS)[28, 29], which forms along the $\tau \cos \theta = -1/6$ curves shown in Fig. 3(a), where the denominator of Eq. (7) vanishes. Except for $\theta = \pm\pi/2$, a HOVHS can be reached by varying the ratio of the first and second neighbor hoppings. In particular, for the bands of tMoTe₂ with $\theta = -2\pi/3$, this occurs for $\tau = 1/3$, shown in the solid line in Fig. 3(a).

Fig. 3(b) displays the Hofstadter spectrum at the HOVHS for $\tau_{\text{HOVHS}} = 1/3$, where a significant reduction in gaps in the range $\nu_h = 1/3, 2/5 \dots, 3/5$ is observed, associated with the collapsing of the scale Δ_{LL} . This feature captures the influence of lattice effects on the structure of composite fermions in Chern bands, in stark contrast with Landau levels [30, 31]. While the role of HOVHS in

promoting competing electronic orders in Chern bands has been recently emphasized[36–39], to our knowledge, the connection between HOVHS and composite fermion states has not received earlier consideration, and is one of the central results of this work.

Remarkably, the proximity to a HOVHS provides a scenario to explore quantum phase transitions induced by closing of the topological gap induced by lattice effects. To test this scenario, we plot in Fig. 3(c) the composite fermion gap of the $\nu_h = 1/3$ state as a function of τ for $\theta = -2\pi/3$ and $t_0 = -1$. In the vicinity of $\tau_{\text{HOVHS}} = 1/3$, we observe that the $\nu_h = 1/3$ gap follows a trend similar to that predicted by Eq.(8), with the gap closing around $\tau \approx 0.3$. The inset shows that this gap closing marks a quantum phase transition between a Jain-FCI ($C = 1$) and a fractal-FCI ($C = -2$) state with Hall conductances $e^2/3h$ and $2e^2/3h$, respectively. We have also observed similar quantum phase transitions for other FCI states such as $\nu_h = 2/5, 3/7$, confirming the generality of the quantum criticality in proximity to a HOVHS.[34]

We stress that topological phase transitions between composite fermion states can take place outside the HOVHS mechanism discussed above. In fact, an important case occurs at $\nu_h = 2/3$, which does not follow the Landau fan emanating from the compressible state at half-filling. In Fig. 4, we trace the composite fermion gap and Hall conductance at $\nu_h = 2/3$ in a wide range of τ . Quantum phase transitions are observed at multiple ratios $\tau = t_1/|t_0|$. Notably, for $-0.74 < \tau < -0.08$, the incompressible state is a Jain-FCI with Hall conductance $2e^2/3h$ topologically consistent with experiments.[6–9] Furthermore, our analysis predicts that interesting behavior may emerge at $\tau \approx -0.08$ due to competition between distinct FCI states, opening new opportunities for experimental and numerical investigations.

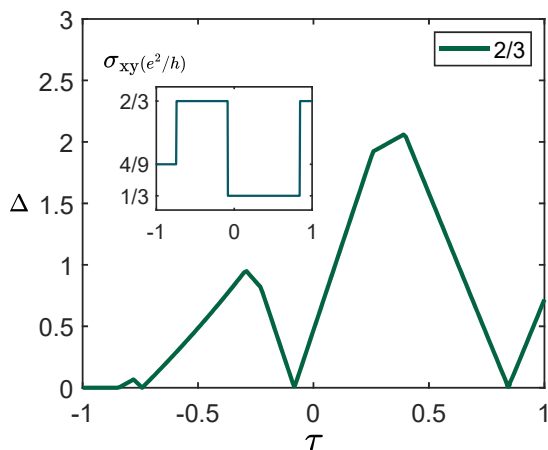


FIG. 4. Composite fermion gap at $\nu_h = 2/3$. $\theta = -2\pi/3$, $t_0 = -1$. The inset plots the phase transition of σ_{xy} . The domain of $\sigma_{xy} = 2/3$ ($\sigma_{xy} = 1/3$) corresponds to $-0.74 < \tau < -0.08$ ($-0.08 < \tau < 0.84$).

Discussion– In summary, employing a composite fermion theory, we have characterized the topological properties of fractional Chern insulators (FCIs) in tMoTe₂. In addition to the experimentally observed FCI states at $2/3$ and $3/5$ fillings, our approach reveals several other candidate FCI states, suggesting new research directions. We highlight the influence of lattice effects on the stability of fractal composite fermion states and their role in inducing quantum phase transitions through higher-order Van Hove singularities. Expanding this approach to characterize FCIs in multilayer graphene heterostructures [40] is a promising avenue. Furthermore, a time-reversal symmetric generalization of the composite fermion approach can shed light on the experimental evidence[41] for the fractional quantum spin Hall effect [42–45] in moiré tMoTe₂. We leave these intriguing questions for future investigation.

Acknowledgments– We are grateful to Andrei Bernevig, Jainendra Jain, and Nicolas Regnault for stimulating discussions. This research was supported by the U.S. Department of Energy, Office of Science, Basic Energy Sciences, under Award DE-SC0023327.

-
- [1] T. Neupert, L. Santos, C. Chamon, and C. Mudry, Phys. Rev. Lett. **106**, 236804 (2011).
 - [2] D. N. Sheng, Z.-C. Gu, K. Sun, and L. Sheng, Nature Communications **2**, 389 EP (2011).
 - [3] E. Tang, J.-W. Mei, and X.-G. Wen, Phys. Rev. Lett. **106**, 236802 (2011).
 - [4] K. Sun, Z. Gu, H. Katsura, and S. Das Sarma, Phys. Rev. Lett. **106**, 236803 (2011).
 - [5] N. Regnault and B. A. Bernevig, Phys. Rev. X **1**, 021014 (2011).
 - [6] J. Cai, E. Anderson, C. Wang, X. Zhang, X. Liu, W. Holtzmann, Y. Zhang, F. Fan, T. Taniguchi, K. Watanabe, *et al.*, Nature **622**, 63 (2023).
 - [7] Y. Zeng, Z. Xia, K. Kang, J. Zhu, P. Knüppel, C. Vaswani, K. Watanabe, T. Taniguchi, K. F. Mak, and J. Shan, Nature **622**, 69 (2023).
 - [8] H. Park, J. Cai, E. Anderson, Y. Zhang, J. Zhu, X. Liu, C. Wang, W. Holtzmann, C. Hu, Z. Liu, *et al.*, Nature **622**, 74 (2023).
 - [9] F. Xu, Z. Sun, T. Jia, C. Liu, C. Xu, C. Li, Y. Gu, K. Watanabe, T. Taniguchi, B. Tong, *et al.*, Physical Review X **13**, 031037 (2023).
 - [10] H. Li, U. Kumar, K. Sun, and S.-Z. Lin, Physical Review Research **3**, L032070 (2021).
 - [11] V. Crépel and L. Fu, Physical Review B **107**, L201109 (2023).
 - [12] C. Wang, X.-W. Zhang, X. Liu, Y. He, X. Xu, Y. Ran, T. Cao, and D. Xiao, Physical Review Letters **132**, 036501 (2024).
 - [13] A. P. Reddy, F. Alsallom, Y. Zhang, T. Devakul, and L. Fu, Physical Review B **108**, 085117 (2023).
 - [14] Y. Jia, J. Yu, J. Liu, J. Herzog-Arbeitman, Z. Qi, H. Pi, N. Regnault, H. Weng, B. A. Bernevig, and Q. Wu, Physical Review B **109**, 205121 (2024).
 - [15] F. Wu, T. Lovorn, E. Tutuc, I. Martin, and A. MacDonald, Physical review letters **122**, 086402 (2019).

- [16] B. I. Halperin and J. K. Jain, *Fractional quantum hall effects: new developments* (World Scientific, 2020).
- [17] E. Y. Andrei, D. K. Efetov, P. Jarillo-Herrero, A. H. MacDonald, K. F. Mak, T. Senthil, E. Tutuc, A. Yazdani, and A. F. Young, *Nature Reviews Materials* **6**, 201 (2021).
- [18] J. K. Jain, *Physical review letters* **63**, 199 (1989).
- [19] A. Lopez and E. Fradkin, *Phys. Rev. B* **44**, 5246 (1991).
- [20] A. Kol and N. Read, *Phys. Rev. B* **48**, 8890 (1993).
- [21] G. Möller and N. R. Cooper, *Phys. Rev. Lett.* **115**, 126401 (2015).
- [22] G. Murthy and R. Shankar, *Phys. Rev. B* **86**, 195146 (2012).
- [23] R. Sohal, L. H. Santos, and E. Fradkin, *Phys. Rev. B* **97**, 125131 (2018).
- [24] J. Wang and L. H. Santos, *Phys. Rev. Lett.* **125**, 236805 (2020).
- [25] F. D. M. Haldane, *Phys. Rev. Lett.* **61**, 2015 (1988).
- [26] D. R. Hofstadter, *Physical Review B* **14**, 2239 (1976), publisher: American Physical Society.
- [27] H. Goldman, A. P. Reddy, N. Paul, and L. Fu, *Phys. Rev. Lett.* **131**, 136501 (2023).
- [28] A. Shtyk, G. Goldstein, and C. Chamon, *Physical Review B* **95**, 035137 (2017).
- [29] N. F. Yuan, H. Isobe, and L. Fu, *Nature communications* **10**, 5769 (2019).
- [30] B. I. Halperin, P. A. Lee, and N. Read, *Physical Review B* **47**, 7312 (1993).
- [31] D. T. Son, *Physical Review X* **5**, 031027 (2015).
- [32] J. Dong, J. Wang, P. J. Ledwith, A. Vishwanath, and D. E. Parker, *Phys. Rev. Lett.* **131**, 136502 (2023).
- [33] In Ref. [15], $t_0 = -0.29$ meV and $t_1 = -0.06$ meV, so that $t_1/t_0 \approx 0.20$.
- [34] See Supplemental Material for details on derivation of the effective Hamiltonian in the presence of Chern-Simons gauge field, Chern-Simons theory of flux attachment and its relation to composite fermions, analytic calculation of the effective mass at half-filling, the Landau-fan close to half-filling and more examples of the correlation between QPT and HOVHS.
- [35] D. J. Thouless, M. Kohmoto, M. P. Nightingale, and M. den Nijs, *Physical Review Letters* **49**, 405 (1982), publisher: American Physical Society.
- [36] P. Castro, D. Shaffer, Y.-M. Wu, and L. H. Santos, *Phys. Rev. Lett.* **131**, 026601 (2023).
- [37] Ö. M. Aksoy, A. Chandrasekaran, A. Tiwari, T. Neupert, C. Chamon, and C. Mudry, *Physical Review B* **107**, 205129 (2023).
- [38] L. Pullasserri and L. H. Santos, *arXiv preprint arXiv:2402.16772* (2024).
- [39] Z. Wu, Y.-M. Wu, and F. Wu, *Physical Review B* **107**, 045122 (2023).
- [40] Z. Lu, T. Han, Y. Yao, A. P. Reddy, J. Yang, J. Seo, K. Watanabe, T. Taniguchi, L. Fu, and L. Ju, *Nature* **626**, 759 (2024).
- [41] K. Kang, B. Shen, Y. Qiu, Y. Zeng, Z. Xia, K. Watanabe, T. Taniguchi, J. Shan, and K. F. Mak, *Nature* **628**, 522 (2024).
- [42] B. A. Bernevig and S.-C. Zhang, *Physical review letters* **96**, 106802 (2006).
- [43] M. Levin and A. Stern, *Physical review letters* **103**, 196803 (2009).
- [44] L. Santos, T. Neupert, S. Ryu, C. Chamon, and C. Mudry, *Physical Review B* **84**, 165138 (2011).
- [45] T. Neupert, L. Santos, S. Ryu, C. Chamon, and C. Mudry, *Physical Review B* **84**, 165107 (2011).

Supplemental Materials

Sec. I describes the Haldane Hamiltonian for the two top bands of tMoTe₂. In Sec. II, we derive the effective Hamiltonian coupled to the Chern-Simons gauge field. Sec. III discussed the Chern-Simons theory of flux attachment and its relation to composite fermions. In Sec. IV, we provide details of the analytical calculation of the effective mass at half-filling ($\nu_h = 1/2$), and perform linear regression on the Hofstadter spectrum close to half-filling. Furthermore, we provide two more examples of Fig. 3(c) at $\nu_h = 2/5, 3/7$.

I. EFFECTIVE HAMILTONIAN IN THE REAL SPACE

We chose nearest neighbor vectors to be $\xi_1 = a(1, 0)$, $\xi_2 = a(-1/2, +\sqrt{3}/2)$, $\xi_3 = a(-1/2, -\sqrt{3}/2)$. Henceforth, $a = 1$. The primitive vectors of the Bravais lattice are $\mathbf{a}_1 = \xi_1 - \xi_2 = (3/2, -\sqrt{3}/2)$ and $\mathbf{a}_2 = \xi_1 - \xi_3 = (3/2, \sqrt{3}/2)$. The lattice vectors are thus $\mathbf{r} = m\mathbf{a}_1 + n\mathbf{a}_2$ with $m, n \in \mathbb{Z}$. We arrange the honeycomb lattice such that $A_{m,n} = \psi_{\mathbf{r}=m\mathbf{a}_1+n\mathbf{a}_2}$ and $B_{m,n} = \psi_{\mathbf{r}+\mathbf{t}_1=m\mathbf{a}_1+n\mathbf{a}_2+\mathbf{t}_1}$, as shown in the Fig. S1.

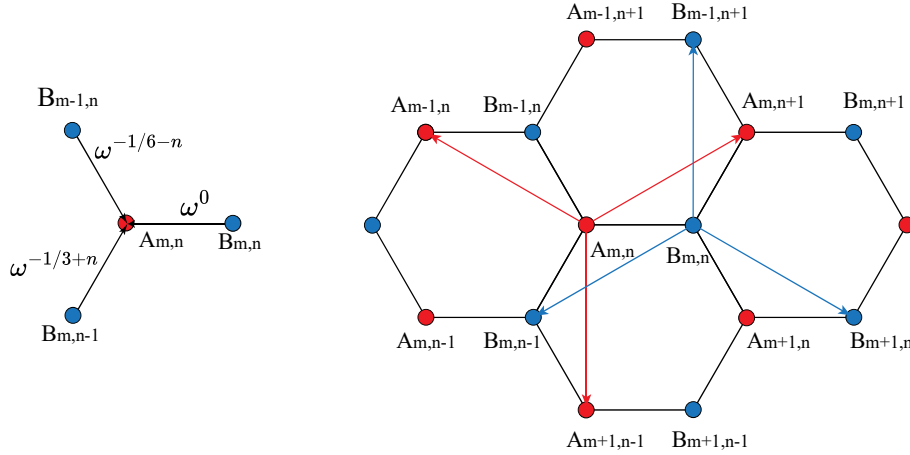


FIG. S1. Left: arrows indicate direction of hopping (i.e. towards site $A_{m,n}$) and the Peierls phase accumulated. Right: arrows indicate direction of NNN hopping amplitude $t_1 e^{i\theta}$. The accumulated Peierls phase in along the NNN hopping can be directly obtained from the phases on the left and the fact that the Aharonov-Bohm phase experience by a charged particle is $e^{\pm i 2\pi \phi_{triangle} / \phi_0}$ where \pm indicates CCW/CW directions and $\phi_{triangle} = \phi_0/6$ is the flux in a triangle that has a blue arrow as one of the edges.

A. Two-band Haldane model

The model contains a NN hopping of strength t_0 and a complex hopping $t_1 e^{i\theta}$ as indicated in Fig. S1 (right),

$$H = H_0 + H_1 \equiv H_0 + H_{AA} + H_{BB}, \quad (\text{S1})$$

where

$$H_0 = t_0 \sum_{m,n} \left(A_{m,n}^\dagger B_{m,n} + A_{m,n}^\dagger B_{m-1,n} + A_{m,n}^\dagger B_{m,n-1} \right) + \text{H.c.}, \quad (\text{S2})$$

$$H_{AA} = t_1 e^{i\theta} \sum_{m,n} \left(A_{m,n+1}^\dagger A_{m,n} + A_{m-1,n}^\dagger A_{m,n} + A_{m+1,n-1}^\dagger A_{m,n} \right) + \text{H.c.} \quad (\text{S3})$$

and

$$H_{BB} = t_1 e^{i\theta} \sum_{m,n} \left(B_{m-1,n+1}^\dagger B_{m,n} + B_{m,n-1}^\dagger B_{m,n} + B_{m+1,n}^\dagger B_{m,n} \right) + \text{H.c.} \quad (\text{S4})$$

Defining the Fourier transform of the fermionic operators as

$$A_{\mathbf{r}} \equiv A_{m,n} = \frac{1}{\sqrt{N}} \sum_{\mathbf{k} \in BZ} e^{i\mathbf{k} \cdot \mathbf{r}} A_{\mathbf{k}}, \quad B_{\mathbf{r}} \equiv B_{m,r} = \frac{1}{\sqrt{N}} \sum_{\mathbf{k} \in BZ} e^{i\mathbf{k} \cdot \mathbf{r}} B_{\mathbf{k}}, \quad (\text{S5})$$

leads to

$$H_0 = \sum_{\mathbf{k}} A_{\mathbf{k}}^\dagger B_{\mathbf{k}} t_0 (1 + e^{-ik_1} + e^{-ik_2}) + \text{H.c.}, \quad (\text{S6})$$

$$H_{AA} = \sum_{\mathbf{k}} A_{\mathbf{k}}^\dagger A_{\mathbf{k}} t_1 e^{i\theta} (e^{-ik_2} + e^{ik_1} + e^{i(-k_1+k_2)}) + \text{H.c.} \quad (\text{S7})$$

$$H_{BB} = \sum_{\mathbf{k}} B_{\mathbf{k}}^\dagger B_{\mathbf{k}} t_1 e^{i\theta} (e^{ik_2} + e^{-ik_1} + e^{i(k_1-k_2)}) + \text{H.c.} \quad (\text{S8})$$

All in all, the model is written as

$$H = \sum_{\mathbf{k}} \begin{pmatrix} A_{\mathbf{k}}^\dagger & B_{\mathbf{k}}^\dagger \end{pmatrix} \begin{pmatrix} t_1 e^{i\theta} (e^{-ik_2} + e^{ik_1} + e^{i(-k_1+k_2)}) + \text{c.c.} & t_0 (1 + e^{-ik_1} + e^{-ik_2}) \\ t_0 (1 + e^{ik_1} + e^{ik_2}) & t_1 e^{i\theta} (e^{ik_2} + e^{-ik_1} + e^{i(k_1-k_2)}) + \text{c.c.} \end{pmatrix} \begin{pmatrix} A_{\mathbf{k}} \\ B_{\mathbf{k}} \end{pmatrix} \quad (\text{S9})$$

II. HOFSTADTER BANDS

Perpendicular to the plane of the lattice we consider is a uniform Chern-Simons field $\mathbf{B} = \nabla \times \mathbf{A}$ and we adopt the gauge $\mathbf{A} = B(x + \sqrt{3}y)\vec{e}_y$. The area of the unit cell is $A_{u.c.} = 3\sqrt{3}/2$ which gives a flux $\phi = B 3\sqrt{3}/2$. With B in the positive direction, this gives a positive counter-clockwise phase $e^{i(q/\hbar) \oint d\mathbf{l} \cdot \mathbf{A}} = e^{i(q/\hbar)\phi} = e^{i2\pi\phi/\phi_0}$, where $\phi_0 = q/\hbar$. Henceforth, we define $\omega = e^{i2\pi\phi/\phi_0}$ and we will be considering the case where $\phi/\phi_0 = p/q$ is a rational number.

We describe the effect of the Chern-Simons gauge field via a Peierls substitution according to

$$t_{\mathbf{r},\mathbf{r}'} \psi_{\mathbf{r}}^\dagger \psi_{\mathbf{r}'} \rightarrow t_{\mathbf{r},\mathbf{r}'} e^{i(2\pi/\phi_0) \int_{\mathbf{r}'}^{\mathbf{r}} d\mathbf{l} \cdot \mathbf{A}} \psi_{\mathbf{r}}^\dagger \psi_{\mathbf{r}'}. \quad (\text{S10})$$

A. Nearest neighbor hopping

Fig. S1 (left) shows the Peierls phases accumulated a charged particle that hops into the $A_{m,n}$ site from its nearest neighbor B sites. This leads to the tight-binding Hamiltonian

$$H_0 = t_0 \sum_{m,n} \left(A_{m,n}^\dagger B_{m,n} + \omega^{-1/6-n} A_{m,n}^\dagger B_{m-1,n} + \omega^{-1/3+n} A_{m,n}^\dagger B_{m,n-1} \right) + \text{H.c.} \quad (\text{S11})$$

We see that the Hamiltonian has an effective translation symmetry $(m, n) \rightarrow (m+1, n+q)$, which embodies the magnetic translation symmetry of the Hamiltonian in the presence of an external magnetic field. Naturally, we extend the unit cell along the \mathbf{a}_2 direction such that the system has a magnetic unit cell with $2 \times q$ sites and the primitive lattice vectors are $\mathbf{a}'_1 = \mathbf{a}_1$ and $\mathbf{a}'_2 = q\mathbf{a}_2$. Accordingly, we define reciprocal lattice vectors of the magnetic BZ as \mathbf{g}'_1 and \mathbf{g}'_2 via $\mathbf{a}'_i \cdot \mathbf{g}'_j = 2\pi\delta_{ij}$, and parameterized momentum via $\mathbf{k} = k_1\mathbf{g}'_1 + k_2\mathbf{g}'_2$.

Letting $n = qr + s$ with $r \in \mathbb{Z}$ and $s = 0, \dots, q-1$, we introduce sublattice operators as

$$A_{m,n} = A_{m,qr+s} \equiv A_{m,r}^{(s)} \equiv A_{\mathbf{R}}^{(s)}, \quad B_{m,n} = B_{m,qr+s} \equiv B_{m,r}^{(s)} \equiv B_{\mathbf{R}}^{(s)}, \quad (\text{S12})$$

where $\mathbf{R} = m\mathbf{a}'_1 + r\mathbf{a}'_2$ is the position of the magnetic unit cell, and their Fourier transforms

$$A_{m,r}^{(s)} = \frac{1}{\sqrt{N}} \sum_{\mathbf{k} \in MBZ} e^{i\mathbf{k} \cdot \mathbf{R}} A_{\mathbf{k}}^{(s)}, \quad B_{m,r}^{(s)} = \frac{1}{\sqrt{N}} \sum_{\mathbf{k} \in MBZ} e^{i\mathbf{k} \cdot \mathbf{R}} B_{\mathbf{k}}^{(s)} \quad (\text{S13})$$

and express each of the terms of the Hamiltonian (S11) as

$$X_1 = \sum_{m,n} A_{m,n}^\dagger B_{m,n} = \sum_{m,r} \sum_{s=0}^{q-1} (A_{m,r}^s)^\dagger B_{m,r}^s = \sum_{\mathbf{k}} \sum_{s=0}^{q-1} (A_{\mathbf{k}}^s)^\dagger B_{\mathbf{k}}^s, \quad (\text{S14})$$

$$X_2 = \sum_{m,n} \omega^{-1/6-n} A_{m,n}^\dagger B_{m-1,n} = \sum_{m,r} \sum_{s=0}^{q-1} \omega^{-1/6-s} (A_{m,r}^s)^\dagger B_{m-1,r}^s = \sum_{\mathbf{k}} \sum_{s=0}^{q-1} \omega^{-1/6-s} e^{-ik_1} (A_{\mathbf{k}}^s)^\dagger B_{\mathbf{k}}^s, \quad (\text{S15})$$

and

$$\begin{aligned} X_3 &= \sum_{m,n} \omega^{-1/3+n} A_{m,n}^\dagger B_{m,n-1} = \sum_{m,r} \sum_{q=0}^{q-1} \omega^{-1/3+s} A_{m,qr+s}^\dagger B_{m,qr+s-1} \\ &= \sum_{m,r} \left[\omega^{-1/3} A_{m,qr}^\dagger B_{m,qr-1} + \sum_{q=1}^{q-1} \omega^{-1/3+s} A_{m,qr+s}^\dagger B_{m,qr+s-1} \right] \\ &= \sum_{m,r} \left[\omega^{-1/3} (A_{m,r}^{(0)})^\dagger B_{m,r-1}^{(q-1)} + \sum_{q=1}^{q-1} \omega^{-1/3+s} (A_{m,r}^{(s)})^\dagger B_{m,r}^{(s-1)} \right] \\ &= \sum_{\mathbf{k}} \left[\omega^{-1/3} e^{-ik_2} (A_{\mathbf{k}}^{(0)})^\dagger B_{\mathbf{k}}^{(q-1)} + \sum_{q=1}^{q-1} \omega^{-1/3+s} (A_{\mathbf{k}}^{(s)})^\dagger B_{\mathbf{k}}^{(s-1)} \right] \end{aligned} \quad (\text{S16})$$

Then the nearest neighbor Hamiltonian $H_0 = t_0 (X_1 + X_2 + X_3) + \text{H.c.}$ then reads

$$\begin{aligned} H_0 &= t_0 \sum_{\mathbf{k}} \sum_{s=0}^{q-1} (1 + \omega^{-1/6-s} e^{-ik_1}) (A_{\mathbf{k}}^s)^\dagger B_{\mathbf{k}}^s + \text{H.c.} \\ & t_0 \sum_{\mathbf{k}} \left[\omega^{-1/3} e^{-ik_2} (A_{\mathbf{k}}^{(0)})^\dagger B_{\mathbf{k}}^{(q-1)} + \sum_{q=1}^{q-1} \omega^{-1/3+s} (A_{\mathbf{k}}^{(s)})^\dagger B_{\mathbf{k}}^{(s-1)} \right] + \text{H.c.} \end{aligned} \quad (\text{S17})$$

B. Next nearest neighbor hopping

The NNN Hamiltonian

$$H_1 = H_{AA} + H_{BB} \quad (\text{S18})$$

corresponds to hopping between equal sublattices.

The AA hopping - with the arrows in Fig. S1 (right) indicates the direction with topological hopping $t_1 e^{i\theta}$ - is given by

$$H_{AA} = t_1 e^{i\theta} \sum_{m,n} \left(\omega^{n+1/2} A_{m,n+1}^\dagger A_{m,n} + \omega^n A_{m-1,n}^\dagger A_{m,n} + \omega^{1-2n} A_{m+1,n-1}^\dagger A_{m,n} \right) + \text{H.c.} \quad (\text{S19})$$

Fourier transforming,

$$\begin{aligned} H_{AA} &= t_1 e^{i\theta} \sum_{\mathbf{k}} \left[\sum_{s=0}^{q-2} \omega^{s+1/2} A_{\mathbf{k}}^{s+1\dagger} A_{\mathbf{k}}^s + \omega^{(q-1)+1/2} e^{-ik_2} A_{\mathbf{k}}^{0\dagger} A_{\mathbf{k}}^{q-1} \right] \\ &+ t_1 e^{i\theta} \sum_{\mathbf{k}} \sum_{s=0}^{q-1} \omega^s e^{ik_1} A_{\mathbf{k}}^{s\dagger} A_{\mathbf{k}}^s \\ &+ t_1 e^{i\theta} \sum_{\mathbf{k}} \left[\omega^1 e^{-ik_1+ik_2} A_{\mathbf{k}}^{q-1\dagger} A_{\mathbf{k}}^0 + \sum_{s=1}^{q-1} \omega^{1-2s} e^{-ik_1} A_{\mathbf{k}}^{s-1\dagger} A_{\mathbf{k}}^s \right] \\ &+ \text{H.c.} \end{aligned} \quad (\text{S20})$$

The BB hopping - with the arrows in Fig. S1 (right) indicates the direction with topological hopping $t_1 e^{i\theta}$ - is given by

$$H_{BB} = t_1 e^{i\theta} \sum_{m,n} \left(\omega^{2n+5/3} B_{m-1,n+1}^\dagger B_{m,n} + \omega^{1/6-n} B_{m,n-1}^\dagger B_{m,n} + \omega^{-1/3-n} B_{m+1,n}^\dagger B_{m,n} \right) + \text{H.c.} \quad (\text{S21})$$

By Fourier transform, we get

$$\begin{aligned} H_{BB} &= t_1 e^{i\theta} \sum_{\mathbf{k}} \left[\sum_{s=0}^{q-2} \omega^{5/3+2s} e^{ik_1} B_{\mathbf{k}}^{s+1\dagger} B_{\mathbf{k}}^s + \omega^{5/3+2(q-1)} e^{ik_1-ik_2} B_{\mathbf{k}}^{0\dagger} B_{\mathbf{k}}^{q-1} \right] \\ &+ t_1 e^{i\theta} \sum_{\mathbf{k}} \left[\sum_{s=1}^{q-1} \omega^{1/6-s} B_{\mathbf{k}}^{s-1\dagger} B_{\mathbf{k}}^s + \omega^{1/6} e^{ik_2} B_{\mathbf{k}}^{q-1\dagger} B_{\mathbf{k}}^0 \right] \\ &+ t_1 e^{i\theta} \sum_{\mathbf{k}} \sum_{s=0}^{q-1} \omega^{-1/3-s} e^{-ik_1} B_{\mathbf{k}}^{s\dagger} B_{\mathbf{k}}^s \\ &+ \text{H.c.} \end{aligned} \quad (\text{S22})$$

III. CHERN-SIMONS THEORY OF FLUX ATTACHMENT

The composite fermion theory characterizes an incompressible state of a partially filled topological band in terms of a band insulator of composite fermions, which are bound states of an electron (or hole) and an even number $2p$ of flux quanta $\phi_0 = h/e = 2\pi$ (in units where $\hbar = e = 1$).

To accomplish the flux attachment, we introduce a Chern-Simons statistical gauge field a_μ and impose the condition

$$(2p) J^\mu = \frac{1}{2\pi} \varepsilon^{\mu\nu\lambda} \partial_\nu a_\lambda, \quad (\text{S23})$$

where J^μ is the number current density. To understand the significance of Eq. S23, consider the $\mu = 0$ equation

$$(2p) J^0 = \frac{1}{2\pi} \varepsilon^{0ij} \partial_i a_j, \quad (\text{S24})$$

where J^0 is the number density. Integrating over space and using Stoke's equation

$$(2p) \int d^2\mathbf{r} J^0 = \frac{1}{2\pi} \int d^2\mathbf{r} \varepsilon^{0ij} \partial_i a_j = \frac{1}{2\pi} \oint \mathbf{a} \cdot d\mathbf{l}. \quad (\text{S25})$$

Since the right hand side gives the Chern-Simons flux divided by the flux quantum (recall $\phi_0 = 2\pi$), this equation establishes that each particle is attached to $2p$ flux quanta.

It turns out that Eq. S23 can be obtained as the Euler-Lagrange equation of motion of a *local* field theory as follows. First, because J^μ is a conserved current, that is $\partial_\mu J^\mu = 0$, it can be expressed in terms of the gradient of a gauge field b_μ as follows,

$$J^\mu \equiv \frac{1}{2\pi} \varepsilon^{\mu\nu\lambda} \partial_\nu b_\lambda. \quad (\text{S26})$$

Eq. S26 describes a particle-vortex duality transformation in $(2+1)$ dimensions.

Consider now the action

$$S_1 = \int d^3x \mathcal{L} = \int d^3x \left(-\frac{2p}{4\pi} \varepsilon^{\mu\nu\lambda} b_\mu \partial_\nu b_\lambda + \frac{1}{2\pi} \varepsilon^{\mu\nu\lambda} a_\mu \partial_\nu b_\lambda \right) \quad (\text{S27})$$

Then, it is straightforward to verify that

$$\frac{\delta S_1}{\delta b_\mu} = 0 \quad \Leftrightarrow \quad \frac{2p}{2\pi} \varepsilon^{\mu\nu\lambda} \partial_\nu b_\lambda = \frac{1}{2\pi} \varepsilon^{\mu\nu\lambda} \partial_\nu a_\lambda, \quad (\text{S28})$$

which is the flux attachment condition Eq. S23.

Now, we write general action that contains fermions and the gauge fields

$$S_2 = \int d^3x \mathcal{L} = \int d^3x \left(\mathcal{L}(\psi^\dagger, \psi, a_\mu) - \frac{2p}{4\pi} \varepsilon^{\mu\nu\lambda} b_\mu \partial_\nu b_\lambda + \frac{1}{2\pi} \varepsilon^{\mu\nu\lambda} a_\mu \partial_\nu b_\lambda \right) \quad (\text{S29})$$

where $\mathcal{L}(\psi^\dagger, \psi, a_\mu)$ is the Lagrangian describing fermions coupled to the statistical gauge field a_μ . When fermions forms a gapped insulator state, integrating out fermions results in a *universal* Chern-Simons response

$$S_3 = \int d^3x \mathcal{L} = \int d^3x \left(\frac{C}{4\pi} \varepsilon^{\mu\nu\lambda} a_\mu \partial_\nu a_\lambda - \frac{2p}{4\pi} \varepsilon^{\mu\nu\lambda} b_\mu \partial_\nu b_\lambda + \frac{1}{2\pi} \varepsilon^{\mu\nu\lambda} a_\mu \partial_\nu b_\lambda \right) \quad (\text{S30})$$

where C is the Chern-number of the fermionic insulator, which in this case is the Chern number of the composite fermion state.

To probe this state's response, we turn on an external probe field A_μ minimally coupled to the charge current $q J^\mu$ ($q = -e$ for the electron) by adding the term $-J^\mu A_\mu = -\frac{1}{2\pi} \varepsilon^{\mu\nu\lambda} A_\mu \partial_\nu b_\lambda$, which results in the action

$$S_4 = \int d^3x \mathcal{L} = \int d^3x \left(\frac{C}{4\pi} \varepsilon^{\mu\nu\lambda} a_\mu \partial_\nu a_\lambda - \frac{2p}{4\pi} \varepsilon^{\mu\nu\lambda} b_\mu \partial_\nu b_\lambda + \frac{1}{2\pi} \varepsilon^{\mu\nu\lambda} a_\mu \partial_\nu b_\lambda - \frac{1}{2\pi} \varepsilon^{\mu\nu\lambda} A_\mu \partial_\nu b_\lambda \right) \quad (\text{S31})$$

We introduce a two-component gauge field

$$a_\mu^I = \begin{pmatrix} b_\mu \\ a_\mu \end{pmatrix}, \quad (\text{S32})$$

and express the action as

$$S_4 = \int d^3x \mathcal{L} = \int d^3x \left(\frac{1}{4\pi} K_{IJ} \varepsilon^{\mu\nu\lambda} a_\mu^I \partial_\nu a_\lambda^J - Q_I \frac{1}{2\pi} \varepsilon^{\mu\nu\lambda} A_\mu \partial_\nu a_\lambda^I \right) \quad (\text{S33})$$

where

$$K = \begin{pmatrix} -2p & 1 \\ 1 & C \end{pmatrix}, \quad Q = \begin{pmatrix} 1 \\ 0 \end{pmatrix} \quad (\text{S34})$$

are, respectively, the symmetric K-matrix and the charge vector.

Integrating out a^I fields gives the response action for the external probe field

$$S_{eff} = \int d^3x \mathcal{L} = -Q^T \cdot K^{-1} \cdot Q \int d^3x \frac{1}{4\pi} \varepsilon^{\mu\nu\lambda} A_\mu \partial_\nu A_\lambda. \quad (\text{S35})$$

From $J^\mu = \frac{\delta S_{eff}}{\delta A_\mu}$, one recovers the Hall conductivity

$$\sigma_{xy} = \frac{C}{2pC + 1}. \quad (\text{S36})$$

IV. COMPOSITE FERMION GAPS CORRELATED WITH EMERGENT HOVHS

A. Effective mass

At half-filling ($\nu_h = 1/2$), $p = 3, q = 1$, the Hamiltonian is 2×2 . The nearest neighbor Hamiltonian reads

$$\begin{aligned} H_0 &= t_0 \sum_{\mathbf{k}} \sum_{s=0}^{q-1} (1 + \omega^{-1/6-s} e^{-ik_1}) (A_{\mathbf{k}}^s)^\dagger B_{\mathbf{k}}^s + \text{H.c.} \\ &+ t_0 \sum_{\mathbf{k}} \left[\omega^{-1/3} e^{-ik_2} (A_{\mathbf{k}}^{(0)})^\dagger B_{\mathbf{k}}^{(q-1)} + \sum_{s=1}^{q-1} \omega^{-1/3+s} (A_{\mathbf{k}}^{(s)})^\dagger B_{\mathbf{k}}^{(s-1)} \right] + \text{H.c.} \\ &= t_0 (1 + \omega^{-1/6} e^{-ik_1} + \omega^{-1/3} e^{-ik_2}) A_{\mathbf{k}}^\dagger B_{\mathbf{k}} + \text{H.c.} \end{aligned} \quad (\text{S37})$$

The AA-hopping reads

$$\begin{aligned}
H_{AA} &= t_1 e^{i\theta} \sum_{\mathbf{k}} \left[\sum_{s=0}^{q-2} \omega^{s+1/2} A_{\mathbf{k}}^{s+1\dagger} A_{\mathbf{k}}^s + \omega^{(q-1)+1/2} e^{-ik_2} A_{\mathbf{k}}^{0\dagger} A_{\mathbf{k}}^{q-1} \right] \\
&\quad + t_1 e^{i\theta} \sum_{\mathbf{k}} \sum_{s=0}^{q-1} \omega^s e^{ik_1} A_{\mathbf{k}}^{s\dagger} A_{\mathbf{k}}^s \\
&\quad + t_1 e^{i\theta} \sum_{\mathbf{k}} \left[\omega^1 e^{-ik_1+ik_2} A_{\mathbf{k}}^{q-1\dagger} A_{\mathbf{k}}^0 + \sum_{s=1}^{q-1} \omega^{1-2s} e^{-ik_1} A_{\mathbf{k}}^{s-1\dagger} A_{\mathbf{k}}^s \right] \\
&\quad + \text{H.c.} \\
&= t_1 e^{i\theta} (\omega^{1/2} e^{-ik_2} + e^{ik_1} + \omega e^{-ik_1+ik_2}) A_{\mathbf{k}}^\dagger A_{\mathbf{k}} + \text{H.c.}
\end{aligned} \tag{S38}$$

The BB-hopping reads

$$\begin{aligned}
H_{BB} &= t_1 e^{i\theta} \sum_{\mathbf{k}} \left[\sum_{s=0}^{q-2} \omega^{5/3+2s} e^{ik_1} B_{\mathbf{k}}^{s+1\dagger} B_{\mathbf{k}}^s + \omega^{5/3+2(q-1)} e^{ik_1-ik_2} B_{\mathbf{k}}^{0\dagger} B_{\mathbf{k}}^{q-1} \right] \\
&\quad + t_1 e^{i\theta} \sum_{\mathbf{k}} \left[\sum_{s=1}^{q-1} \omega^{1/6-s} B_{\mathbf{k}}^{s-1\dagger} B_{\mathbf{k}}^s + \omega^{1/6} e^{ik_2} B_{\mathbf{k}}^{q-1\dagger} B_{\mathbf{k}}^0 \right] \\
&\quad + t_1 e^{i\theta} \sum_{\mathbf{k}} \sum_{s=0}^{q-1} \omega^{-1/3-s} e^{-ik_1} B_{\mathbf{k}}^{s\dagger} B_{\mathbf{k}}^s \\
&\quad + \text{H.c.} \\
&= t_1 e^{i\theta} (\omega^{5/3} e^{ik_1-ik_2} + \omega^{1/6} e^{ik_2} + \omega^{-1/3} e^{-ik_1}) B_{\mathbf{k}}^\dagger B_{\mathbf{k}} + \text{H.c.}
\end{aligned} \tag{S39}$$

Collecting previous terms leads to the 2x2 Hamiltonian is

$$H[k_1, k_2, \theta, t_0, t_1] = \begin{pmatrix} H_{AA} & H_0 \\ H_0^* & H_{BB} \end{pmatrix} = h_0(\mathbf{k}) \sigma_0 + \sum_{i=1}^3 h_i(\mathbf{k}) \sigma_i, \tag{S40}$$

with

$$\begin{aligned}
h_0(\mathbf{k}) &= 2t_1 \cos \theta (\cos k_1 - \cos k_2 + \cos(k_1 - k_2)) \\
h_1(\mathbf{k}) &= t_0 (1 - \cos k_1 + \cos k_2) \\
h_2(\mathbf{k}) &= t_0 (-\sin k_1 + \sin k_2) \\
h_3(\mathbf{k}) &= 2t_1 \sin \theta (-\sin k_1 - \sin k_2 + \sin(k_1 - k_2))
\end{aligned} \tag{S41}$$

The energy of the lower band is directly obtained

$$\varepsilon_-(\mathbf{k}) = \frac{H_{AA} + H_{BB}}{2} - \frac{1}{2} \sqrt{(H_{AA} - H_{BB})^2 + 4H_0 H_0^*} = h_0(\mathbf{k}) - |\mathbf{h}(\mathbf{k})|. \tag{S42}$$

At $k_1 = -p \cdot \frac{\pi}{3}, k_2 = -p \cdot \frac{2\pi}{3}, E_{\text{low}}$ reaches the minimum, i.e.

$$\begin{aligned}
\partial_{k_1} \varepsilon_-(\mathbf{k}) &= \partial_{k_2} \varepsilon_-(\mathbf{k}) = 0 \\
\partial_{k_1}^2 \varepsilon_-(\mathbf{k}) &= \partial_{k_2}^2 \varepsilon_-(\mathbf{k}) = \frac{2}{3} |t_0| + 4t_1 \cos(\theta) \\
\partial_{k_1} \partial_{k_2} \varepsilon_-(\mathbf{k}) &= -\frac{1}{3} |t_0| - 2t_1 \cos(\theta)
\end{aligned} \tag{S43}$$

Expanding $\varepsilon_-(\mathbf{k})$ around the minimum,

$$\varepsilon_-(\mathbf{k}) = \varepsilon_-^* + \frac{1}{2} \left(\frac{2}{3} |t_0| + 4t_1 \cos(\theta) \right) \begin{pmatrix} k_1 & k_2 \end{pmatrix} \begin{pmatrix} 1 & -1/2 \\ -1/2 & 1 \end{pmatrix} \begin{pmatrix} k_1 \\ k_2 \end{pmatrix} \tag{S44}$$

Considering $\mathbf{k} = \frac{k_1}{2\pi}\vec{g}_1 + \frac{k_2}{2\pi}\vec{g}_2$, with $\vec{g}_1 = \frac{4\pi}{3}(1/2, -\sqrt{3}/2)$ and $\vec{g}_2 = \frac{4\pi}{3}(1/2, \sqrt{3}/2)$, gives

$$\begin{pmatrix} k_x \\ k_y \end{pmatrix} = \frac{1}{3} \begin{pmatrix} 1 & 1 \\ -\sqrt{3} & \sqrt{3} \end{pmatrix} \begin{pmatrix} k_1 \\ k_2 \end{pmatrix} \leftrightarrow \begin{pmatrix} k_1 \\ k_2 \end{pmatrix} = \begin{pmatrix} 3/2 & -\sqrt{3}/2 \\ 3/2 & \sqrt{3}/2 \end{pmatrix} \begin{pmatrix} k_x \\ k_y \end{pmatrix} \quad (\text{S45})$$

resulting in the rotationally invariant parabolic expansion

$$\varepsilon_-(\mathbf{k}) = \varepsilon_-^* + \frac{1}{2} \left(\frac{2}{3}|t_0| + 4t_1 \cos(\theta) \right) \begin{pmatrix} k_x & k_y \end{pmatrix} \begin{pmatrix} 9/4 & 0 \\ 0 & 9/4 \end{pmatrix} \begin{pmatrix} k_x \\ k_y \end{pmatrix} \quad (\text{S46})$$

from which

$$\varepsilon_{\text{eff}} = \frac{\hbar^2}{2m^*} k^2 = \left(\frac{3}{4}|t_0| + \frac{9}{2}t_1 \cos(\theta) \right) k^2 \quad (\text{S47})$$

yields the effective mass in Eq. (7).

Following the same approach of Eq. (8), we can approximate the slopes of the energy bands in the Landau-fan asymptotically close to the half-filling ($\nu_h = 1/2$) according to

$$E_n = E^* + (n + 1/2)\hbar\omega_c = E^* + (n + 1/2)\frac{4}{3\sqrt{3}}\Phi_0\frac{\hbar e}{m^*}|\nu_h - 1/2| \Rightarrow dE_n/d\nu_h = \pm(n + 1/2)\frac{4}{3\sqrt{3}}\Phi_0\frac{\hbar e}{m^*} \quad (\text{S48})$$

To compare the slopes in Eq. (S48) with the Hofstadter spectrum, we perform linear regression on the lowest three bands in the Hofstadter spectrum close to the half-filling at $\theta = -2\pi/3, t_0 = -1, t_1 = -0.2$ as shown in Fig. S2.

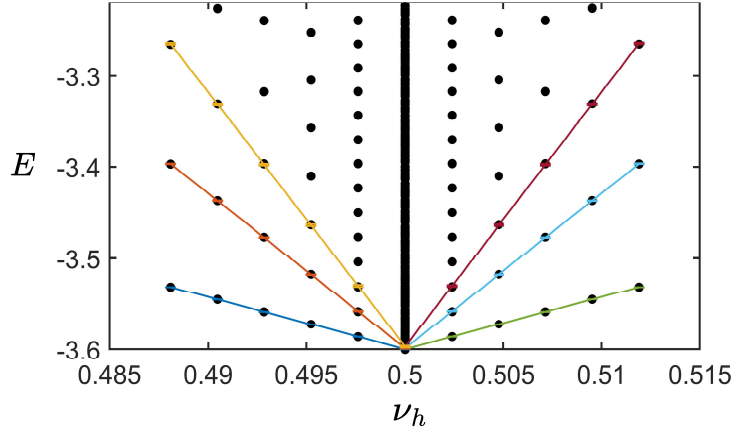


FIG. S2. Linear regression of the lowest three bands in the Landau-fan at $\theta = -2\pi/3, t_0 = -1, t_1 = -0.2$. Solid dots are the Hofstadter spectrum, solid lines with error bars show the linear regression.

The fitting result compared with Eq. (S48) is summarized in Table. S1, their agreement supports the Landau-fan picture accounted by the effective mass at half-filling.

Landau level index	Landau-fan Slope		Eq. (S48)
	Linear regression		
	$\nu_h < 1/2$	$\nu_h > 1/2$	
$\Delta E_0 = (0 + 1/2)\hbar\omega_c$	-5.7128 ± 0.0107	5.7171 ± 0.0099	± 5.8042
$\Delta E_1 = (1 + 1/2)\hbar\omega_c$	-16.9621 ± 0.0523	16.9793 ± 0.0488	± 17.4125
$\Delta E_2 = (2 + 1/2)\hbar\omega_c$	-27.8583 ± 0.1342	27.9012 ± 0.1256	± 29.0208

TABLE S1. The Landau-fan slopes from linear regression and predicted by Eq. (S48) at $\theta = -2\pi/3, t_0 = -1, t_1 = -0.2$.

B. QPT correlated with HOVHS for $\nu_h = 2/5, 3/7$

Here we present two more examples of Fig. 3(c) closer to the half-filling at $\nu_h = 2/5, 3/7$ (in Fig. S3) to show that the correlation between QPTs and HOVHS is extensive in the Jain-FCI states.

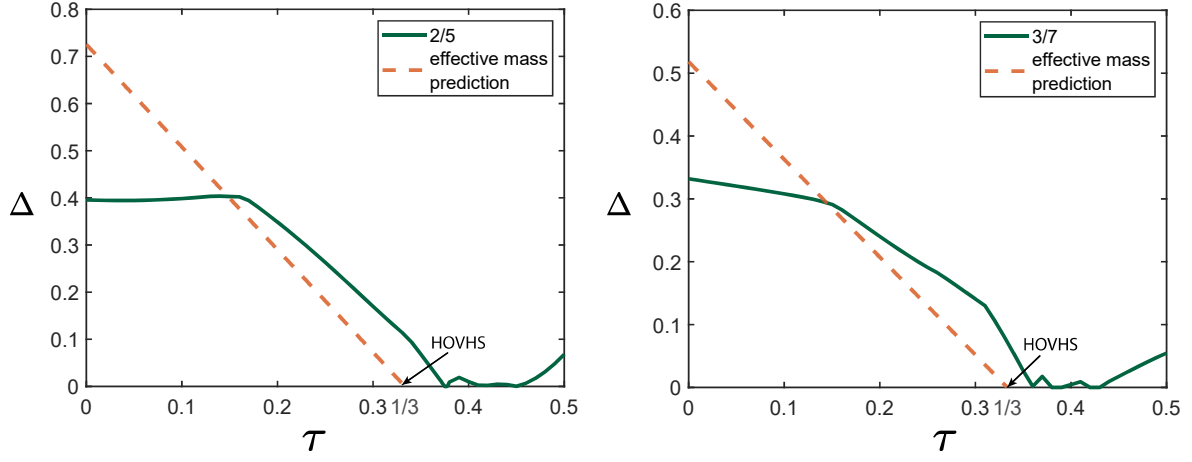


FIG. S3. $\sigma = -1, \theta = -2\pi/3, t_0 = -1$. The composite fermion gap versus τ . left: $\nu_h = 2/5$, right: $\nu_h = 3/7$. The green curve shows the gap, the orange line shows the gap predicted for each hole filling by effective mass at $\nu_h = 1/2$ which vanishes at $\tau = 1/3$ as the HOVHS emerges.